Proceedings of ASME Turbo Expo 2022
Turbomachinery Technical Conference and Exposition
GT2022
June 13-17, 2022, Rotterdam, The Netherlands

GT2022-81921

NUMERICAL INVESTIGATION OF POTENTIAL FLOW INDUCED VIBRATIONS OF STEAM TURBINE LAST STAGE ROTOR AT LOW LOAD OPERATION - PART 2: ROTATING INSTABILITIES DETECTION

Tommaso Diurno*, Antonio Andreini, Bruno Facchini

Department of Industrial Engineering
University of Florence, Florence, Italy
Email: tommaso.diurno@htc.unifi.it

Nicola Maceli, Lorenzo Arcangeli

Baker Hughes
Florence, Italy

ABSTRACT

Steam turbines play an important role in global power generation since they are widely used, as thermal engines, in fossil-fueled, nuclear, and concentrated solar power plants. Therefore, recent trends in steam turbine design practices are closely related to the development of the energy market, which is especially focused on expansion of fast renewable energy. As a direct consequence, due to intrinsic variability of the green-energy resources, the steam turbines address the need to increase their flexibility to ensure the stable functioning of the power grid. Greater flexibility is linked to even increasing Low Volume Flow (LVF) operating conditions which could trigger dangerous non-synchronous aerodynamic excitations of the last stage bucket (LSB). In order to discover the source of such excitations, an extensive numerical study, presented in a two-part publication, has been carried out to investigate two different mechanisms potentially accountable for flow induced vibrations. In part one, the focus is on the flutter stability, while the present part deals with the detection of rotating instability phenomena that might arise in the last stage during LVF conditions. Such aerodynamic instabilities are investigated using CFD simulations by performing 3D, Unsteady Reynolds Averaged Navier Stokes (URANS) of the low pressure, last turbine stage coupled with an axial exhaust hood, with structural struts. The full annulus mesh of both the last stage and diffuser is considered with the transient stator-rotor interface to properly account for unsteady interaction effects.

The influence of the operating conditions on the fluid dynamic behavior is assessed by considering six different operating conditions, starting from the design condition and gradually decreasing the mass flow rate. The presence of rotating instabilities is demonstrated by monitoring the fluid dynamic variables during the simulation and by using advanced post-processing techniques, such as Proper Orthogonal Decomposition (POD).

Keywords: Steam Turbine, Exhaust System, CFD, Unsteady, Flow-Induced Vibration, Low Volume Flow, Rotating Instability, POD.

NOMENCLATURE

Acronyms

BPF	Blade Passing Frequency
CSP	Concentrated Solar Power
CFD	Computational Fluid Dynamics
EO	Ratio between frequency and rotational frequency
FFT	Fast Fourier Transform
GCI	Grid Convergence Index
LEOF	Low Engine Order Frequency
LSB	Last Stage Bucket
LVF	Low Volume Flow
OP	Operating Point

*Address all correspondence to this author.

POD Proper Orthogonal Decomposition
REV Number of rotor mesh revolution
RIF Rotating Instability Frequency
URANS Unsteady Reynolds Average Navier-Stokes

INTRODUCTION

Steam turbines are widely used for electric power generation in several configurations, ranging from conventional power plants, such as fossil-fueled, nuclear plants, to green energy based Concentrated Solar Power (CSP) systems. The most recent trends in steam turbine design practice are, therefore, strongly related to the development of the energy market, which is even more oriented towards a fast renewable energy expansion; indeed, according to IEA [1], renewable sources will overtake coal becoming the largest source of electricity generation in 2025. In 2020 the global share of renewables in electricity generation was almost 25% and, despite the economic uncertainties due to pandemic, according to IRENA's [2] estimations, it is likely to increase up to 37% in 2030, and up to 86% in 2050.

Due to the intrinsic variability of green energy resources, and absence of commercially available, and cost-effective storage systems, steam turbines operating in conventional power plants, must increase their operational flexibility to ensure stability of the power grid. Higher operational flexibility involves continuous start-up and shut-down of the machine and therefore frequent low load operations, also known as low volume flow (LVF) conditions, characterized by the ventilation of the Last Stage Bucket (LSB). During such conditions, the LSB may experience non-synchronous aerodynamic excitations triggered by the surrounding fluid. The dynamic stresses induced by these phenomena can be extremely dangerous since they are superimposed to the stresses caused by centrifugal forces. In light of the above, and due to very high cost associated with experiments, the integration of a numerical procedure in the design process to characterize the unsteady fluid behavior during LVF conditions is of primary importance.

During the LVF condition, the flow field in the last stage presents the characteristic behavior shown in Figure 1. The low reaction at the hub implies that such a section is the first one affected by the reduction of the volume flow, indeed, the flow can not pass through the root of the blades and it is centrifuged towards the tip generating a separation region in the diffuser behind the rotor blades. In this condition, the blade tip acts as a compressor leading to the onset of the tip torus vortex in the figure shown in Figure 1. As demonstrated in this work and by many authors in the literature, the circumferential tip torus vortex may lead to non-synchronous aerodynamic excitations of the LSB; and is also known as Rotating Instability (RI).

One of the first pieces of evidence of flow induced vibration during LVF condition is presented by Shnee Et al. [3,4] with experimental measurements obtained by monitoring the LSB with

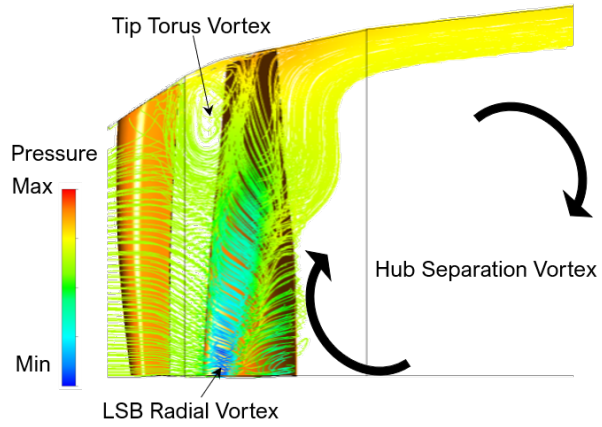

FIGURE 1: Characteristic flow field in LSB during LFV, © 2022 Baker Hughes Company - All rights reserved.

strain gauges during low load operations. The measurements highlighted a peak in blade stresses 2-3 times higher compared to the design case. Schmidt et al. [5] contributed on this topic by using unsteady pressure probes in a four-stage air turbine showing the peak of pressure fluctuations in a volume flow between 10 and 25% respect to the design one.

W. Gerschutz et al [6] carried out an experimental investigation on two different three-stage low-pressure steam turbines during LVF conditions, with flow rates between 0 and 30% of the design. In order to capture the unsteady pressure fluctuations, fast response probes were developed while the blade stresses were measured using the strain gauges. As far as the structural behavior is concerned, the study reported strong vibrations in the first turbine, triggered by aerodynamic excitations at the resonant frequency of the second mode, at measured mass flow rate of 13% of the design flow. From a fluid dynamics point of view, high amplitude disturbances were measured in a frequency range between 4 and 8 times the rotational frequency.

Segawa et al. [7] investigated a four-stage low pressure model steam turbine under low-load conditions (load between 0-20% of design value). Pressure fluctuations were measured with transducers at inner and outer casing walls and on stationary blades. The results show how the pressure fluctuations get higher in both outer and inner casing by decreasing the volumetric flow in all the stages, except for L3 (first low-pressure stage). A good agreement in the reversed flow region between experiment and numerical simulations, was reported by Seeno et al. [8]. Considering the 20% load case, both experiment and CFD show pressure oscillations only after the last stage. Since any tip torus vortex is shown in this operating condition is possible to conclude that such oscillations are generated by the interaction between reverse flow and through flow in the hub separation vortex (schematically shown in Figure 1) behind the rotor blades.

Blade vibrations linked to the hub separation vortex have been also reported by Zhou et al. [9]. The experimental and numerical results presented in this work show how the hub separation vortex leads to Low Engine Order Frequency (LEOF) disturbances which are responsible for the LSB first axial mode excitation.

In the last decades, computational fluid dynamics (CFD) has become crucial for the analysis of the flow field during LVF conditions. However, the transient flow field which characterizes these conditions is extremely computationally demanding and correct assumptions are crucial in order to reduce the numerical costs. The most commonly employed is the steady state assumption, that was used in early numerical studies on this topic by Herzog et al. [10]. The comparison with the experiment revealed that RANS simulations were able to catch the main features of the flow field. Steady state assumption has been also used by Sigg et al. [11], the comparison with experiments showed a qualitatively good agreement in the pressure ratio across the stages and in the last stage power output prediction. However, the RANS simulation fails to predict the detailed spanwise distribution of the flow field most likely due to a coarse mesh and transient effects not being captured by a steady state simulation.

Considering the inherent unsteadiness of the flow at these conditions, it seems clear that, for in-depth knowledge, steady state simulations are of limited use and unsteady CFD simulations are required. In this regard, Zang et al. [12] carried out unsteady simulations to observe the basic features of the RI in the same low-pressure steam turbine already studied by Sigg et al. [11]. The study is based on unsteady 2D calculations of the entire annulus multi-passage. Although the flow field in this operating condition has a strong radial component, as highlighted by the streamlines in Figure 1, a 2D blade-to-blade approach was used to reduce the computational effort. The 2D assumption is significant, since it does not consider 3D flow features, which could be essential for the onset of the RI. However, the RI was still detected, meaning that 3D phenomena, such as tip clearance vortex, are not the key features to trigger the RI. Subsequent investigation by the same authors [13] performed a 3D unsteady simulation with the low-pressure turbine and the exhaust diffuser. The main objective of the work was to understand the role of the exhaust system in the onset of the RI. The authors demonstrated how the large-scale separation of the diffuser is not linked to the onset of the RI since this separation is also present in an operating condition outside the instability range. The authors of the study suggest that a more likely cause of the instability onset may be the compressor mode operation of the blade tip, as observed in other research [6, 10, 11].

In light of the already mentioned studies, the vibration of the rotor blade seems to be connected with two possible mechanisms. The first one is linked to pressure fluctuations in the tip region of the axial gap between the last stator and rotor blades, with the so-called RI, while the other with pressure fluctuations linked to unsteady phenomena that may arise in the hub separation vortex behind the rotor blade.

In order to understand the link between pressure fluctuations and blade vibrations, N. Shibukawa et al. [14] performed a series of experiments on a test rig consisting of a 10 MW steam turbine last stage akin to a large size nuclear power plant. The experimental results identified maximum stresses occurring when the axial velocity decreases to between 25-30% of the design operating point. Such a condition is characterized by the maximum pressure rise across the LSB tip, in line with previous investigations [6]. However, according to the study results, this condition is not only sufficient, but necessary. Indeed, another operating point, characterized by a similar pressure rise across the last stage blade tip, presents a low level of vibrations. The unsteady pressure signals at the last stage nozzle exit tip end wall have been post-processed with FFT and the results show how the pressure fluctuation can excite the blades, and its frequency depends on the steam condition. The operating point characterized by maximum vibration stress coincides with the highest pressure oscillations at the nozzle exit tip end wall. In a subsequent investigation presented by N. Shibukawa et al. [15] the measurements were instead performed on a six-stage full scale steam turbine. The study compared the relationship between pressure fluctuations and blade vibrations, and showed how the nozzle exit pressure fluctuations are a good indicator of the blade vibrations. On the other hand, the rotor exit failed to predict the blade vibration trend. Concerning the rotor hub region, a much different behavior between pressure fluctuations and blade vibration is reported meaning that the flow unsteadiness in the separation area behind the blade has less potential to trigger blade vibrations probably due to the high blade stiffness in such region.

The CFD investigations presented up to this point are characterized by strong assumptions in the numerical setup. The most limiting assumption are steady-state, 2D or 3D periodic fluid domain simplifications. The first attempt to simulate the full 3D annulus of the last stage coupled with a simplified exhaust hood has been presented by Megerle et al. [16]. The unsteady CFD simulations were carried with the commercial code CFX [17] with the k-ε turbulence model and wall function to limit the number of near-wall computational nodes. Although both the experiment and numerical model were done with air, in place of steam, the existence of the RI was still demonstrated, meaning that this phenomenon is not linked to the fluid type. In addition, two different exhaust geometries are tested in order to evaluate the effect of different boundary conditions on the investigated phenomenon to show how the outlet boundary affects the number of the RI stall cells. This trend is expected since the number of cells is stochastic, while their rotational speed is comparable and not sensitive to outlet type. Also the effect of the tip clearance is evaluated, and in contrast with the results presented by Gerschutz et al. [6], the number of cells and their rotational speed seem to be insen-

sitive to such flow phenomenon. Comparing with experiments, the author reported differences in the fractional speed of the stall cells.

The following numerical study presented by Megerle et al. [18] considers steam, with ideal gas assumption, and a real geometry exhaust hood. These results demonstrated again that a real exhaust configuration is necessary to capture the amplitude of the pressure fluctuations, while the triggering of the rotating instability seems to be unaffected by the exhaust type. Despite the differences in the geometry and in the fluid used in the previous work, the tip RI is found for a similar value of the flow coefficient, between 0.04 and 0.15. It can be concluded that the flow coefficient is a key parameter to investigate this phenomenon. A discrepancy in the fractional speed between numerical prediction and experiment was also reported in this work. In order to enhance the numerical accuracy, a scale-resolving turbulence modeling, Scale Adaptive Simulation (SAS) approach, has been used by Megerle et al. [19] to simulate large-scale turbulent fluctuations. The comparison between URANS, SAS and experiments shows small differences between the numerical models in resolving the flow field and both fail to predict the axial velocity near the casing, most likely attributed to using a coarse mesh. Significant differences between the numerical models are instead reported by considering the Short Time Fourier Transform (STFT) of a static pressure time history on a monitor point located between stator and rotor at 87% span, where SAS shows a higher level of unsteadiness over the entire range of frequencies. The SAS model is able to predict a two-band behavior of the rotating instability at low frequency, which means that two RI patterns are present simultaneously.

Further developments in the numerical modeling of the LVF conditions are proposed by Ercan and Vogt [20] by carrying out improved Delayed Detached Eddy Simulations (iDDES). In this work, a comparison between URANS, iDDES and experiments in different operating conditions is presented, characterized by 6,3%, 12% and 18% of the design mass flow. The fluid domain consists of 3 stages with a full annulus extension and a radial exhaust hood. The tip gap is included in the fluid domain and the steam is modelled as an ideal gas. Both the CFD models agree quite well with experiments for the lower mass flow cases while failing to predict the lower frequency instabilities at 18% mass flow. The improvements achieved with the iDDES are linked to the tendency to show more RI configurations due to the instabilities of the flow field generated by the turbulence effects.

The focus of the current work is aimed at expanding the knowledge of flow induced vibration mechanism during LVF conditions and answering one of the fundamental questions, which arise in this engineering problem (stated by Megerle et al. [16]). The question is whether the link between the fluid and the structure should be considered an aero-mechanical (e.g. blade fluttering), or a purely fluid dynamic phenomenon. In order to explain this question, an extensive numerical study, presented in a two-part publication, has been carried out to investigate two different mechanisms potentially accountable for flow induced vibrations. The first part of this work [21], focused on the blade-fluttering, has allowed to exclude this aero-mechanical mechanism as a potential source of vibration in low load conditions, in agreement with what has recently been shown experimentally by Bessone et al. [22] and numerically by Pinelli et al. [23]. The second part of the present work is instead focused on the purely aerodynamic instabilities by carrying out unsteady simulations on a full annulus last stage coupled with a real geometry axial diffuser of a steam turbine manufactured by Baker Hughes for Concentrated Solar Power (CSP) system applications.

To the author's knowledge, few previous studies are available in the literature concerning axial exhaust systems during LVF conditions, and this is the first time that they are being investigated with unsteady simulations. Recently Hoznedl et al. [24] presented experimental and steady state numerical results of flow in the LSB of a steam turbine with an axial diffuser. Temperature and pressure measurements highlight how the steam at L1 inlet is superheated during LVF conditions. This justifies the ideal gas assumption adopted in many investigations [18, 19, 20]. They also demonstrated how a flow coefficient of 0.17 is the transition point for the ventilation of the last stage. Furthermore, by analyzing the trend of blade vibration as a function of the flow coefficient, it is worth mentioning that the blade vibration experiences a significant increase corresponding to a flow coefficient of 0.27, where the hub separation appears in the diffuser. Such a vibration may be triggered by the flow unsteadiness in the hub separation vortex. The blade vibration increase continuously by decreasing the flow coefficient in the region of ventilation (pressure ratio at the tip higher than 1) up to reach a maximum in correspondence of a flow coefficient of 0.05 with the maximum pressure rise across the blade tip. This peak of vibration may be due to the presence of the RI. Further decrease of the flow coefficient beyond this value leads to a decrease of blade vibration.

COMPUTATIONAL METHODS

The CFD simulations presented in this work have been carried out with the commercial Navier–Stokes solver ANSYS CFX [17]. The turbulence effects have been modeled by using the SST k-ω model [25] combined with automatic wall treatment, which automatically switches from a standard wall function approach to a low Reynolds formulation as the y+ value changes. This turbulence model was developed to offer improved predictions of separated flow and is therefore suitable for modeling strongly separated flow as demonstrated by Bardina et al. [26].

A bounded high-resolution scheme has been employed to calculate the advection fluxes of continuity, momentum and total energy equations, resulting in second-order accuracy. In order to reduce the computational costs, steam is considered as an ideal

gas in light of findings of previous investigations, which demonstrated that during LVF conditions, the steam is superheated due to the ventilation effect [18, 24].

The CFD setup with two different fluid domains including periodic and full 3D, both with rotor tip clearance, is shown in Figure 2. The periodic model uses the mixing plane approach, which only requires to model a single blade passage by performing a circumferential averaging of the fluxes through the interface, allowing significant savings in computational time due to reduced mesh size and the steady-state assumption [27]. A single last stage passage, with the mixing plane interface, coupled with a periodic slice of the diffuser offers a very good trade off between accuracy and computational costs when applied in the aerodynamic investigation of the exhaust systems [28]. In addition, several investigations have shown the applicability of RANS simulation to capture the characteristic flow features during LVF conditions [10, 11]. This is the reason why this setup was used to perform a mesh sensitivity study; and to examine the evolution of the flow field as a consequence of reducing the mass flow. This assessment has allowed to discover the most interesting operating points to be simulated with the full 3D unsteady approach.

The 3D domain considers a full annulus mesh of both the last stage and the axial exhaust hood (Figure 3), with struts included since the real geometry of the diffuser seems necessary to accurately predict the amplitude of pressure fluctuations [18]. In order to capture the flow unsteadiness the stator-rotor transient interface available in CFX, coupled with the rotor moving mesh has been used. Additional full 3D RANS simulations with the frozen rotor interfaces have been carried out to initialize unsteady calculations.

The URANS simulations have been solved with a second-order backward Euler scheme and a time step of 2.3e-5 [s], resulting in the rotor mesh taking 15 steps per pitch angle, which is sufficient to properly capture the blade passing effect, as reported by Fu et al. [29]. Consequently, the selected time step can be used to detect both the tip RI, which present a characteristic frequency far below the blade passing frequency [18, 20], and the hub separation vortex disturbances which appear at even lower frequencies [9]. The total physical time simulated is averagely equal to 10 complete rotor revolutions (REV), which in some cases is essential to properly capture all the unsteady flow features. The exact number of rotor revolutions depends on the operating condition. Due to the large size of the fluid domain mesh and long physical time being simulated, the average computational cost of each unsteady simulation is almost 100K CPU hours.

As a convergence criterion for the unsteady simulations the summation of the resultant force on all blades has been considered, with a convergence target of relative oscillation below 3%. Additional time steps were carried out based on the author's experience in order to collect sufficient transient data for the post-processing.

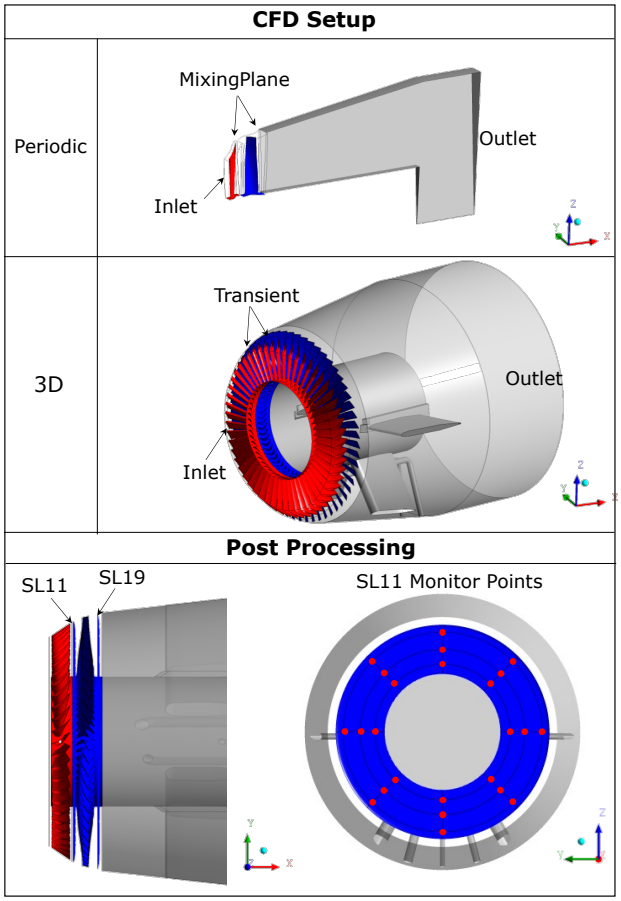

FIGURE 2: Numerical setup and post processing surfaces. © 2022 Baker Hughes Company - All rights reserved.

The selection of the monitor points and post-processing surfaces plays a key role in the identification of transient instabilities. A schematic representation of the monitor points used in this work is depicted in Figure 2. There is a total of 48 monitor points, which are spaced on two different rotor surfaces, at 3 different span sections (20%, 50%, 85%) and in 8 angular positions. Each monitor point records the transient history of static and total pressure in both relative and absolute frames of reference. In addition, the average surface pressure, the resultant force and the torque of 4 different rotor blades have been monitored.

Despite using significant number of monitor points, the analysis of a local signal may lead to information loss from the data. For this reason the 2D pressure fields, in plane SL11 and SL19 (see Figure 2) have also been stored to perform more in-depth post-processing based on Proper Orthogonal Decomposition (POD). Such a technique, proposed by Lumley [30], applied to fluid dynamic allows the decomposition of a complex flow

field into several modes, ordering them according to their energy content. The graphical representation of each mode enables the identification of coherent structures within a turbulent flow, which are often embedded, favoring the understanding of how they interact and how they contribute to the development of a specific phenomenon.

In the present work the so called Snapshot proper orthogonal decomposition (POD) proposed by Sirovinch [31, 32] has been implemented with a Matlab script. This technique is a development of the theory presented by Lumley [30]. The mathematics explanation of POD is out of the scope of this work and can be found in the references [31,32]. For a detailed description of this method applied to fluid dynamic problems, it is worth mentioning the work presented by Berkooz et al. [33]. Recently POD has been successfully applied to turbomachinery applications by D. Lengani et al. [34, 35, 36, 37, 38], where the technique is used to identify coherent structures in low pressure turbine cascade in order to investigate the loss generation mechanism.

The exhaust hood computational grid was generated with ANSYS meshing [39], it is composed of tetrahedral elements in the free stream, with a local mesh refinement near the struts, where high gradients are expected. In order to sufficiently resolve the boundary layer, 20 prismatic elements are used near the walls to obtain a y+ value of approximate 1.5. For the computational grid of the blade rows, ANSYS TURBOGRID was used to generate a hexahedral mesh. The clearance region in the rotor blade was resolved with two additional grid blocks, one for each side of the airfoil in the tip section of the blade, connected with general grid interface (GGI).The computational grids of both turbine stage and diffuser are shown in 3.

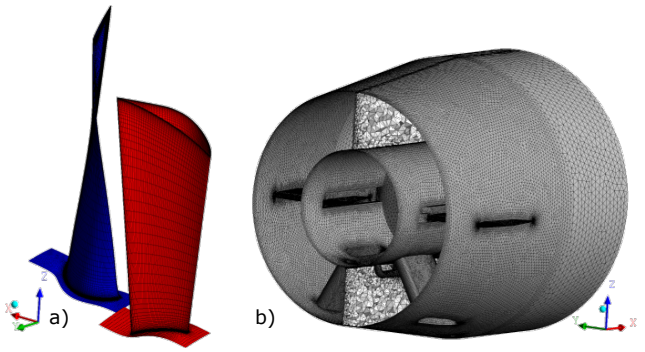

FIGURE 3: Single passage and entire diffuser mesh. © 2022 Baker Hughes Company - All rights reserved.

The total number of elements of 600 K for the periodic model, which increases to 42 M for the 3D model by replicating the single stage mesh over the 360° extension, has been obtained using the mesh sensitivity study by applying the grid convergence index (GCI) method proposed by Roache [40]. Such a method is based on the generalized theory of Richardson extrapolation and involves the comparison of discrete solutions at three different grids spacing with coarse, medium and fine mesh refinements. A detailed description of the application of the GCI method method can be found in reference [41]. The results of using this procedure to perform a rotor mesh sensitivity study are presented in Figure 4, where the normalized integral blade pressure is plotted versus representative mesh spacing. The results prove that the discrete solutions converge monotonically as the grid is refined and the medium size mesh meets the convergence requirements required by the procedure.

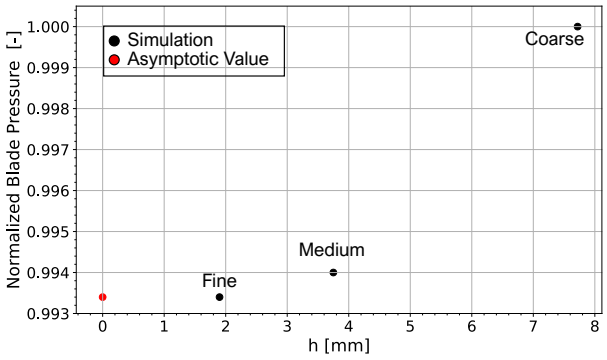

FIGURE 4: Rotor Mesh sensitivity.
© 2022 Baker Hughes Company - All rights reserved.

For the boundary conditions, a total pressure, total temperature and flow direction profile have been imposed at the inlet. The velocity profiles are calculated with the multi-stage steady state calculation presented in the part 1 of this work [21], while the average static pressure is imposed at the outlet section. In order to study the evolution of the flow field during LVF condition, six different operating point (OP) conditions, summarized in Table 1, have been investigated.

The mass flow ($\overline{m}$) and axial velocity ($\overline{U_{ax}}$) at the diffuser inlet are normalized by the design value, while the swirl angle, calculated as the arctangent of the ratio between tangential and axial velocity at the diffuser inlet, is normalized by OP4 value (maximum swirl condition).

The flow coefficient ϕ is defined as the ratio between axial velocity at the diffuser inlet and the tangential rotor speed at the mean radius. The OPs have been selected with two different strategies: TEST A starts from the off-design point and decreases the condenser pressure up to reaching a safe condition within the stability range, while TEST B starts from the design condition (OP0) and gradually increases the condenser pressure up to unsafe operations from the stability range. It is worth highlighting how OP1 and OP4, and OP5 presents flow coefficients within the range of instability identified by both Megerle et al. [18] and Hoznedl et al. [24].

TABLE 1: Investigated operating conditions. © 2022 Baker Hughes Company - All rights reserved.

OP	TEST	$\overline{m}$ [-]	$\overline{U_{ax}}$ [-]	ϕ [-]	$\overline{\theta}$ [-]
OP0	B	1	1	0.52	0
OP1	A	0.224	0.195	0.10	0.96
OP2	A	0.375	0.375	0.25	0.73
OP3	B	0.653	0.653	0.16	0.87
OP4	B	0.322	0.322	0.06	1
OP5	B	0.522	0.522	0.13	0.92

RESULTS

The evaluation of six different operating conditions defines the application limits of the investigated steam turbine, and is graphically illustrated in Figure 5. Among these operating points, OP1 and OP4 are defined as unsafe conditions, due to the presence of strong unsteadiness in the flow field, that may trigger blade vibrations. In order to gradually characterize the transient behavior of the instabilities, the numerical results of the simulations are presented starting with TEST A followed by TEST B.

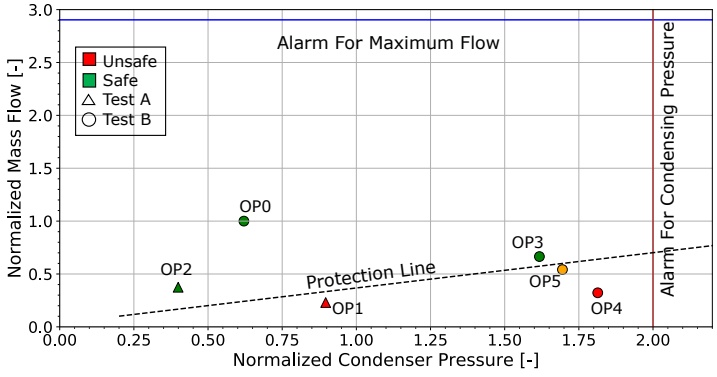

FIGURE 5: Steam turbine application limits. © 2022 Baker Hughes Company - All rights reserved.

As discussed previously, in the numerical setup section, TEST A is obtained by directly simulating a low load condition (OP1) and then decreasing the condenser pressure to reach a stable operating condition (OP2). The results are presented in Figure 6, in terms of FFT spectra of the pressure signals recorded in the (relative-frame) monitor points presented in Figure 2.

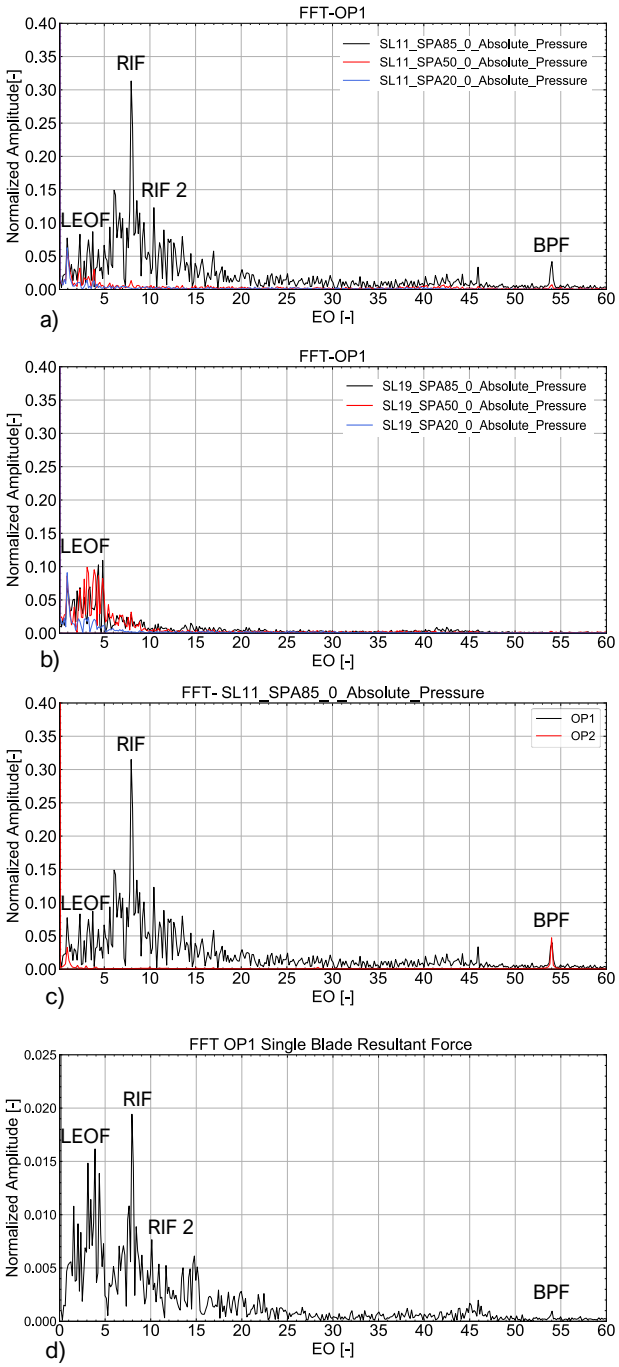

FIGURE 6: FFT spectra of relative monitor point pressure signal a) Effect of Spanwise location in the OP1 and surface SL11, b) Effect of Spanwise location in the OP1 and surface SL19, c) Comparison between OP1 and OP2 in surface SL11 at 85% span, d) FFT spectrum of a single blade resultant force. © 2022 Baker Hughes Company - All rights reserved.

In this work, the amplitude of the pressure signal is normalized by a reference value, while the frequency is normalized by the rotational value (EO), and the physical time is normalized by the time to complete one rotor revolution (REV).

In the naming convention used for the monitor points (see Figure 2), the first code (e.g. "SL11") indicates the streamwise location of the post-processing surfaces, the second code shows the spanwise location (e.g. "SPA85" is 85% of the span) and finally, the last number indicates the circumferential location (e.g. "0" is theta=0 coincident with y axis).

In Figure 6a, the FFT spectra of the pressure signal at 3 different span locations for a fixed stream-wise location is presented. From this plot the higher level of unsteadiness of the tip section (at 85% span) is immediately apparent. In particular, a very strong peak of amplitude of 8 EO can clearly be seen. As will be demonstrated later, this peak is due to the presence of a rotating instability (RI) at the tip of the region between stator and rotor blades, and the reason why it is referred as RIF (Rotating Instability Frequency). In line with the results presented in the literature, the amplitude of the RIF is well above the stator blade wake, referred to as BPF (Blade Passing Frequency). In addition, other low engine order frequency (LEOF) disturbances can be seen in the spectra, which are attributed to diffuser asymmetry generated by the structural struts and to the hub separation vortex illustrated in Figure 1.

The LEOFs are also clearly discernible in Figure 6b, where the FFT spectra of the pressure on the surface SL19, between rotor blades and diffuser, are shown; while the RIF is no longer so evident. It is worth highlighting that the amplitude of LEOF is well distinguishable in all the spectra, meaning that in contrary to RI this phenomenon affects a wide section of the span.

Specifically, the effect of the diffuser asymmetry at 1 EO is the same on the 3 signals since this is due to the presence of full-span structural struts only in the lower part of the diffuser, as shown in Figure 3. Figure 6c shows the effect of a different operating condition on the pressure signal in a monitor point located in the tip section of the SL11 surface. By looking at this graph it is clear how both the RIF and LEOF, except for the 1 EO linked to the diffuser asymmetry, disappear by decreasing the condenser pressure, while the stator wake effect amplitude is slightly stronger due to the higher mass flow of the OP2. For the sake of brevity, the effect of different circumferential locations of the monitor point is not presented, but it is worth mentioning how the signal of the RI is almost the same over the entire full annulus extension.

Finally, the FFT spectrum of the blade resultant force is reported in Figure 6d. From looking at this graph it is clearly evident that both the RI and the LEO instabilities observed in the pressure signals have a direct impact on the blade force, since the same characteristic frequencies are clearly distinguishable.

As observed by previous investigations [19, 20], the RI is inherently unstable and changeable in time and for this reason, a

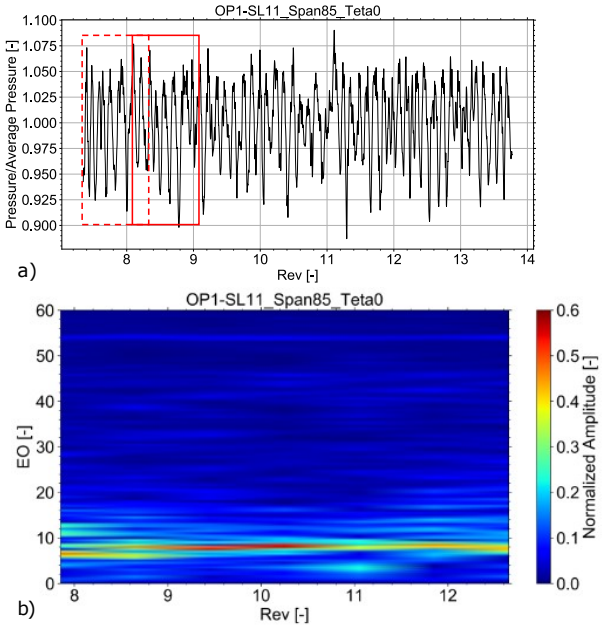

FIGURE 7: a) Pressure transient history with FFT moving windows (in red), b) STFT spectra of pressure signal. © 2022 Baker Hughes Company - All rights reserved.

STFT (Short Time Fourier Transform) is useful to study the evolution of the transient signal in the physical time. In figure 7b the STFT of the OP1 pressure signal at 85% of the SL11 surface is reported. The STFT is realized by considering a moving FFT window of 1 REV with an overlapping interval of 0.2 REV, as illustrated in Figure 7a. As can be seen by the STFT the signal of the RI is not constant in time, contrary to the stator wake visible at the top of the contour at 54 EO with a constant signal. Specifically, in the first part of the time window considered, between 8 and 9 REV, the RI signal is clearly visible with a characteristic frequency of 6 EO while in the final part of the time window, between 9 and 12 REV, the dominant frequency is shifted to 8 EO. In addition, another weaker signal of instability is visible at 11 EO, which owing to POD, is associated with another RI configuration. Also the unsteadiness at LOEFs are present in this spectrogram with an unstable signal, between 2 and 4 EO, which reaches a maximum of amplitudes around 11 REV.

To gain a deeper understanding of the unsteady flow field in the SL11 surface, a POD analysis of the pressure field has been realized by processing a series of 1740 snapshots allowing the identification of the dynamics related to the different source of unsteadiness observed in the FFT spectra. The time difference between each snapshot is equal to 2 time steps which determines a total time of 4 REV. A snapshot of the pressure field and the POD results are presented in Figure 8a and Figure 8b,c,d respectively.

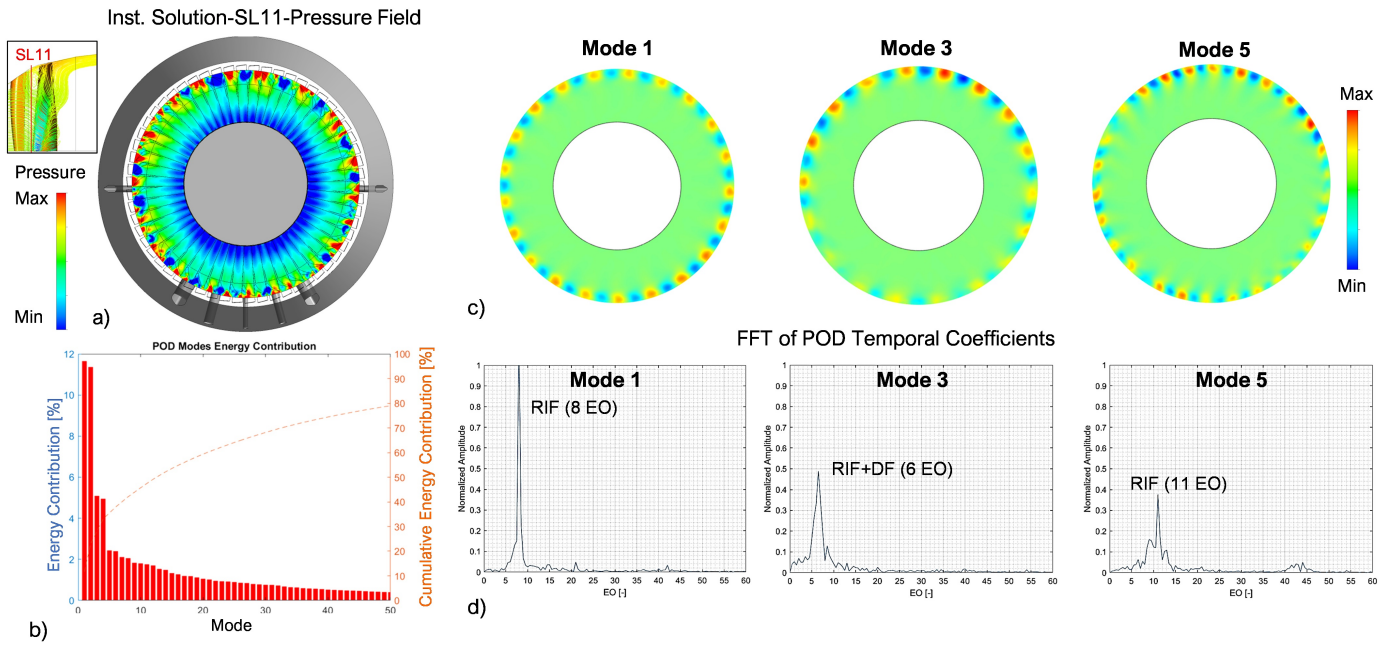

FIGURE 8: a) OP1 instantaneous pressure field on SL11 , b) POD modes energy contribution, c) Statistical POD Modes spatial distribution, d) FFT spectra of POD modes temporal coefficients. © 2022 Baker Hughes Company - All rights reserved.

In the snapshot of the pressure field, the stall cells near the casing can be seen. Such flow structures, by rotating in the circumferential direction with a fraction of the rotor speed, lead to the pressure oscillation observed in Figure 6. However, due to the instability of the signal shown in STFT this pattern shown by the snapshot is not stable in time, in this regard POD can be used for the identification of spatio-temporal evolution of this flow feature. As clarified in the numerical setup section, the POD is an energy based decomposition that is aimed at determining the best approximation of a data set with a series of modes, each of which is characterized by spatial and temporal distribution and by its energy content. Figure 8b shows the singular and cumulative energy content of each POD mode. Since the energy is a measure of the importance of each mode, it can be concluded that the first and second POD modes largely contribute to the resultant pressure field. The statistical spatial distribution of POD modes is presented in Figure 8c, in which mode 1 is the principal mode that is exactly the graphical representation of the RI. Furthermore, 16 stall cells pattern with a dominant frequency of 8 EO (RIF) are clearly visible in Figure 8d, from both the spectrum of the POD temporal coefficients, and from the FFT spectra of pressure signal of the monitor point in Figure 6a. Mode 2 is not reported since it has the same dominant frequency, similar energy content and a shifted spatial distribution, which is typical behavior of convective flow [38] and is also valid for modes 3-4 and modes 5-6. In the spatial distribution of mode 3, the already presented 16 stall cells pattern is still observable, however in this case there is a non-uniformity between the upper and the lower part of the surface. In particular, the stall cells in the upper part are more intense compared to the cells on the lower part. This effect leads to a shift of the characteristic frequency of the mode from 8 EO to 6 EO, already observed in STFT in Figure 7, and it may be related to the geometric asymmetry induced by the diffuser. Finally, in mode 5 another RI pattern with a different number of pressure cells can be observed, which confirms the hypothesis of the temporal instability phenomenon. A similar dual RI configuration has been already reported in previous studies [6, 19, 20].

The results of TEST B are reported in Figure 9 with the FFT spectra of all the operating points and in Figure 10 with a specific focus on the OP4 which shows the RI and high LEO unsteadiness. Figure 9a reports the FFT spectra in the 85% span of the SL11 surface, with presence of the RI discussed previously for OP1. At the operating point OP4 it's evident and worth highlighting that the characteristic frequency of such instability is different than OP1. This is in line with the findings of previous studies [15, 18, 19, 20] which have already demonstrated that the RIF is related to the operating conditions. In addition, Figure 9a illustrates the FFT spectrum of the design point OP0, in line with expectations it is characterized by only a peak in amplitude corresponding to BPF, while OP3 and OP5 show only a very weak unsteadiness located in the low frequency region, meaning that

the RI is not present at these conditions.

By looking at Figure 9b very strong unsteadiness at LOEFs can be seen, as expected from TEST A results discussion, such instabilities are generated in the hub separation area behind the rotor blades and they are maximum in the OP4. For an in-depth explanation of this phenomenon, a POD analysis has been carried out on the SL19 surface by using 1740 snapshots of the pressure field.

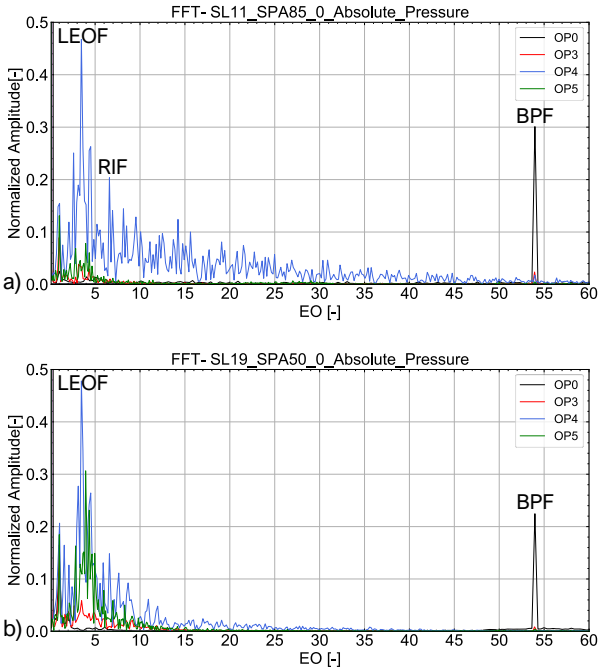

FIGURE 9: FFT spectra of relative pressure signal a) Effect of Spanwise location for all the OPs of TEST B at the tip of surface SL11, b) Effect of Spanwise location for all the OPs of TEST B at the mid of surface SL19. © 2022 Baker Hughes Company - All rights reserved.

The results of the POD analysis are reported in Figure 10b,c,d together with a singular snapshot in Figure 10a. By looking at the pressure field in Figure 10a, a 6 pressure cells pattern can be easily seen. The rotation of these cells in circumferential direction leads to the low-frequency instabilities observed previously and reported in Figure 9. These pressure cells are the cores of the helical vortices, generated due to the high swirl of the flow. These cores are located between the through flow and the reverse flow, as highlighted by the isoline at zero axial velocity in Figure 10a, where there is a very high tangential velocity gradient. This gradient is generated by the interaction between the highly swirled flow that crosses the LSB

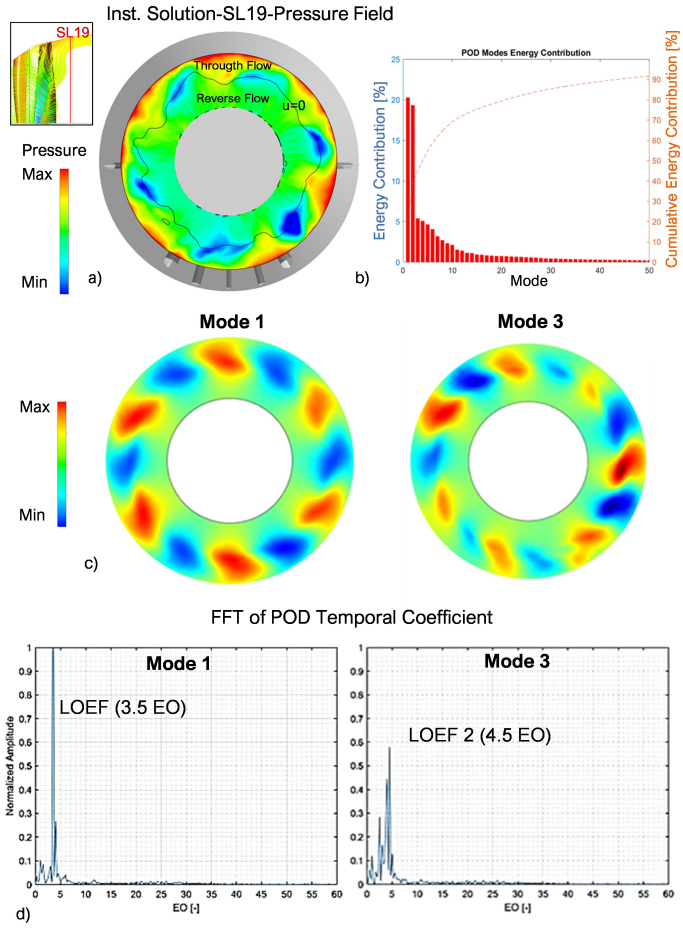

FIGURE 10: a) OP4 instantaneous pressure field on SL19, b) POD modes energy contribution, c) Statistical POD Modes spatial distribution, d) FFT spectra of POD modes temporal coefficients. © 2022 Baker Hughes Company - All rights reserved.

tip and the hub separation vortex schematically shown in Figure 1.

The central role of the swirl in this phenomenon is also confirmed by examining the reported data for OP1, OP4 and OP5, which are operating points characterized by the higher swirl angle and all experience discernible pressure oscillations in the low-frequency region. This instability mechanism may be attributed to the Precessing Vortex Core (PVC) observed in several fluid dynamic applications. Aleeksenko et al. [42] described the formation of helical vortices in strongly swirled flow and in presence of separation, which may develop a rotation in the circumferential direction. The theory of helical vortices specifies how their number may depend on several factors, as confirmed by looking at the FFT spectra of OP4 and OP5 in Figure 9 where

a slightly different dominant frequency in the low-frequency region can be seen, meaning that there is a different number of vortices. In addition, these vortices are not stationary and their number may vary in time [42]. This is confirmed by the POD analysis in Figure 10c where, by comparing mode 1 with mode 3 it is clear how the number of pressure cells, and consequently their dominant frequency, can vary during the transient evolution of the flow field. Concerning the modes' energy content, modes 1 and 2 largely contribute to the resultant pressure field since they are accountable for 40% of the global energy content. The spatial distribution of mode 1 clarifies how this phenomenon affects a significant part of the span, contrary to the RI which is located only near the blade tip. However, the span extension and the amplitude of the pressure oscillations are strongly linked to the operating conditions, and in particular to the swirl number. Indeed, by decreasing the swirl this phenomenon becomes weaker for the OP5 and OP1, and totally disappears in the other operating points.

The present work enabled the identification of a mechanism of instabilities linked to the hub separation vortex, alternative to the tip RI widely observed in literature. The findings of this study are also in line with numerical and experimental evidence proposed in the literature [7, 9, 24], which reported an increase of blade vibration related to the onset of the hub separation vortex in the diffuser.

CONCLUSION

Renewable energy expansion poses significant challenges in the steam turbine design practice due to the increase of LVF conditions. Such conditions are extremely dangerous for the low pressure turbine blades, which may consequently experience flow-induced vibrations. In this context, an extensive numerical study has been realized to understand the cause of these potential vibrations. The first part of this work [21], focused on the blade flutter at low load conditions, has excluded this phenomenon as a possible cause. The second part, reported in this work, has finally allowed understanding of the potential fluid dynamic mechanisms capable of triggering the blade vibrations.

A simplified periodic model, based on the steady state assumption, and mixing plane as frame change type has been utilized to perform a mesh sensitivity study. Subsequently, a limited number of simulations, at conditions of interest, was assessed with full 3D unsteady numerical setup. The latter consisted of a full annulus mesh of the last stage of a low pressure turbine coupled with a real geometry axial diffuser, with structural struts included.

Six operating conditions have been simulated with the 3D setup to identify turbine application limits aimed at avoiding unsafe operating conditions, characterized by strong pressure oscillations in the LSB which may trigger vibrations.

The rotating instability accountable for a significant part of this pressure oscillation has been detected in the tip region between stator and rotor. The strong link between pressure oscillations and alternating blade loads has been clarified by monitoring the blade force. The FFT spectrum of a single blade force has revealed the same peaks observed in the pressure signals.

A graphical representation of this instability has been presented thanks to the POD which allows decomposing a complex flow field into different modes, ranked by their energy content. In this case, the RI is manifested with a 16 pressure cells pattern, which counter rotates (opposite rotor motion) at a fraction of the speed. The tip RI mechanism is line with other studies found in literature [16, 18, 19, 20]. In addition, the application of 2D POD has allowed avoiding the potential loss of information linked to a post processing based on local monitor points.

The RI is not the only source of unsteadiness detected in this work, which agrees with other investigations [7, 9, 24], as the low-frequency instabilities behind the rotor blades are revealed. These instabilities are generated by the interaction between the hub separation vortex in the diffuser and the strongly swirled flow at the outlet of the rotor, confined at the tip. The high-velocity gradient between through and reverse flow leads to the onset of helical vortices, with the vortex core located in the zero velocity separation line, which rotates with a mechanism similar to the ones observed for the tip RI.

Consistent with the helical vortex theory reported in the literature [42], the number of vortices may vary in the time since they are inherently unstable. In addition, this work demonstrates how the intensity of this phenomenon is correlated with the swirl angle at the rotor outlet, and consequently to the operating condition, since it affects the velocity gradient.

In future studies, 3D POD can be used to gain deeper understanding of the presented phenomena and also allow investigation of the axial extension of the manifested instabilities. The implementation of such a technique is primarily limited by the large amount of data that needs to be processed in this application. Furthermore, in order to improve the numerical accuracy, hybrid RANS-LES can be used to allow better understanding of the role of turbulence in the described phenomena.

REFERENCES

[1] IEA, 2020. "Renewables 2020".

[2] IRENA, 2020. "Global renewables outlook: Energy transformation 2050".

[3] Y. Shnee, F. Ponomarev, M. F., and Bystritskii, L., 1971. "Features of operation of a turbine stage with low dm/l ratio under conditions of low loads". *Teploenergetika,* ***18***, pp. 39 – 42.

[4] Y. Shnee, O. Ponomarev, V. S. M. Z., and Fedorov, M., 1974. "Influence of the operational factors on dynamic stresses in moving blades of a turbine stage". *Teploenergetika,* ***21***, pp. 49 – 52.

[5] Schmidt, D., and Riess, W., 1999. "Steady and unsteady flow measurements in the last stages of lp steam turbines". In IMECHE CONFERENCE TRANSACTIONS, Vol. 1, MECHANICAL ENGINEERING PUBLICATIONS, pp. 723–734.

[6] Gerschütz, W., Casey, M., and Truckenmüller, F., 2005. "Experimental investigations of rotating flow instabilities in the last stage of a low-pressure model steam turbine during windage". *Proceedings of the Institution of Mechanical Engineers, Part A: Journal of Power and Energy,* ***219***(6), pp. 499–510.

[7] Segawa, K., Senoo, S., Hamatake, H., Kudo, T., Nakamura, T., and Shibashita, N., 2012. "Steady and unsteady flow measurements under low load conditions in a low pressure model steam turbine". In International Conference on Nuclear Engineering, Vol. 44977, American Society of Mechanical Engineers, pp. 833–839.

[8] Senoo, S., Segawa, K., Hamatake, H., Kudo, T., Nakamura, T., and Shibashita, N., 2011. "Computations for unsteady compressible flows in a multistage steam turbine with steam properties at low load operations". *Journal of engineering for gas turbines and power,* ***133***(10).

[9] Zhou, B., Mujezinovic, A., Coleman, A., Ning, W., and Ansari, A., 2011. "Forced response prediction for steam turbine last stage blade subject to low engine order excitation". In Turbo Expo: Power for Land, Sea, and Air, Vol. 54679, pp. 2447–2453.

[10] Herzog, N., Gu¨ ndogdu, Y., Kang, G., Seume, J., and Rothe, K., 2005. "Part load operation of a four-stage turbine". In Turbo Expo: Power for Land, Sea, and Air, Vol. 47306, pp. 663–672.

[11] Sigg, R., Heinz, C., Casey, M., and Sürken, N., 2009. "Numerical and experimental investigation of a low-pressure steam turbine during windage". *Proceedings of the Institution of Mechanical Engineers, Part A: Journal of Power 19 and Energy,* ***223***(6), pp. 697–708.

[12] Zhang, L., He, L., and Stüer, H., 2013. "A numerical investigation of rotating instability in steam turbine last stage". *Journal of turbomachinery,* ***135***(1).

[13] Zhang, L., He, L., and Stüer, H., 2012. "3-d time domain unsteady computation of rotating instability in steam turbine last stage". In Turbo Expo: Power for Land, Sea, and Air, Vol. 44724, American Society of Mechanical Engineers, pp. 559–567.

[14] Shibukawa, N., Tejima, T., Iwasaki, Y., Murakami, I., and Saito, I., 2011. "A correlation between vibration stresses and flow features of steam turbine long blades in low load conditions". In Turbo Expo: Power for Land, Sea, and Air, Vol. 54679, pp. 2437–2446.

[15] Shibukawa, N., Iwasaki, Y., and Watanabe, M., 2013. "Unsteady flow features and vibration stresses of an actual size steam turbine last stage in various low load conditions". In Turbo Expo: Power for Land, Sea, and Air, Vol. 55201, American Society of Mechanical Engineers, p. V05BT25A030.

[16] Megerle, B., Stephen Rice, T., McBean, I., and Ott, P., 2013. "Numerical and experimental investigation of the aerodynamic excitation of a model low-pressure steam turbine stage operating under low volume flow". *Journal of engineering for gas turbines and power,* ***135***(1).

[17] ANSYS-CFX-Solver, 2019. "Theory guide". *Release l9.1*.

[18] Megerle, B., McBean, I., Stephen Rice, T., and Ott, P., 2014. "Unsteady aerodynamics of low-pressure steam turbines operating under low volume flow". *Journal of turbomachinery,* ***136***(9), p. 091008.

[19] Megerle, B., Rice, T. S., McBean, I., and Ott, P., 2015. "Turbulent scale resolving modelling of rotating stall in low-pressure steam turbines operated under low volume flow conditions". In Turbo Expo: Power for Land, Sea, and Air, Vol. 56796, American Society of Mechanical Engineers, p. V008T26A016.

[20] Ercan, I., and Vogt, D. M., 2021. "Detached eddy simulation of rotating instabilities in a low-pressure model steam turbine operating under low volume flow conditions". In Turbo Expo: Power for Land, Sea, and Air, Vol. 85017, American Society of Mechanical Engineers, p. V008T22A006.

[21] Pinelli, L., Mariotti, F., Arnone, A., Marconcini, M., and Arcangeli, L., 2022. "Numerical investigation of flow induced vibrations of steam turbine last stage rotor at low load operation – part 1: Sensitivity to flutter occurrence". *[Manuscript submitted for publication], ASME 2022.*

[22] Bessone, A., Guida, R., Marrè Brunenghi, M., Patrone, S., Carassale, L., Kubin, Z., Arnone, A., and Pinelli, L., 2020. "Aeromechanical characterization of a last stage steam blade at low load operation: Part 1—experimental measurements and data processing". In Turbo Expo: Power for Land, Sea, and Air, Vol. 84218, American Society of Mechanical Engineers, p. V10AT24A019.

[23] Pinelli, L., Vanti, F., Peruzzi, L., Arnone, A., Bessone, A., Bettini, C., Guida, R., Marré Brunenghi, M., and Slama, V., 2020. "Aeromechanical characterization of a last stage steam blade at low load operation: Part 2—computational modelling and comparison". In Turbo Expo: Power for Land, Sea, and Air, Vol. 84218, American Society of Mechanical Engineers, p. V10AT24A017.

[24] Hoznedl, M., Sedlák, K., Mrózek, L., Dadáková, T., Kubín, Z., and Gregor, K., 2020. "Experimental and numerical study of flow and dynamics on lsb at 34 mw steam turbine". In Turbo Expo: Power for Land, Sea, and Air, Vol. 84201, American Society of Mechanical Engineers, p. V009T23A003.

[25] Menter, F. R., 1994. "Two-equation eddy-viscosity turbulence models for engineering applications". *AIAA journal,*

32(8), pp. 1598–1605.

[26] Huang, P., Bardina, J., and Coakley, T., 1997. "Turbulence modeling validation, testing, and development". *NASA technical memorandum,* ***110446***, p. 147.

[27] Diurno, T., Fondelli, T., Nettis, L., Maceli, N., Arcangeli, L., Andreini, A., and Facchini, B., 2020. "Numerical investigation on the aerodynamic performance of a low-pressure steam turbine exhaust hood using design of experiment analysis". *Journal of Engineering for Gas Turbines and Power,* ***142***(11).

[28] Diurno, T., Tomasello, S. G., Fondelli, T., Andreini, A., Facchini, B., Nettis, L., and Arcangeli, L., 2021. "Development of a design approach for the optimization of steam turbine exhaust system performance through cfd modelling". In Turbo Expo: Power for Land, Sea, and Air, Vol. 85017, American Society of Mechanical Engineers, p. V008T22A013.

[29] Fu, J.-L., Liu, J.-J., and Zhou, S.-J., 2011. "Unsteady Interactions Between Axial Turbine and Nonaxisymmetric Exhaust Hood Under Different Operational Conditions". *Journal of Turbomachinery,* ***134***(4), 07. 041002.

[30] Lumley, J. L., 2007. *Stochastic tools in turbulence*. Courier Corporation.

[31] Sirovich, L., 1987. "Turbulence and the dynamics of coherent structures. i. coherent structures". *Quarterly of applied mathematics,* ***45***(3), pp. 561–571.

[32] Sirovich, L., 1989. "Chaotic dynamics of coherent structures". *Physica D: Nonlinear Phenomena,* ***37***(1-3), pp. 126–145.

[33] Berkooz, G., Holmes, P., and Lumley, J. L., 1993. "The proper orthogonal decomposition in the analysis of turbulent flows". *Annual review of fluid mechanics,* ***25***(1), pp. 539–575.

[34] Lengani, D., and Simoni, D., 2015. "Recognition of coherent structures in the boundary layer of a low-pressure-turbine blade for different free-stream turbulence intensity levels". *International Journal of Heat and Fluid Flow,* ***54***, pp. 1–13.

[35] Lengani, D., Simoni, D., Ubaldi, M., Zunino, P., and Guida, R., 2016. "Turbulence production, dissipation and length scales in laminar separation bubbles". In 11th International ERCOFTAC Symposium on Engineering Turbulence Modelling and Measurements, Sicily, Italy, Sept, pp. 21–23.

[36] Lengani, D., Simoni, D., Ubaldi, M., Zunino, P., Bertini, F., and Michelassi, V., 2017. "Accurate estimation of profile losses and analysis of loss generation mechanisms in a turbine cascade". *Journal of Turbomachinery,* ***139***(12), p. 121007.

[37] Davide, L., Simoni, D., Ubaldi, M., Zunino, P., and Bertini, F., 2017. "Coherent structures formation during wake-boundary layer interaction on a lp turbine blade". *Flow, Turbulence and Combustion,* ***98***(1), pp. 57–81.

[38] Lengani, D., Simoni, D., Pichler, R., Sandberg, R., Michelassi, V., and Bertini, F., 2019. "On the identification and decomposition of the unsteady losses in a turbine cascade". *Journal of Turbomachinery,* ***141***(3), p. 031005.

[39] ANSYS, 2019. "Ansys meshing user's guide". *Release l9.1*.

[40] Roache, P. J., 1998. *Verification and validation in computational science and engineering*, Vol. 895. Hermosa Albuquerque, NM.

[41] Fondelli, T., Diurno, T., Palanti, L., Andreini, A., Facchini, B., Nettis, L., Arcangeli, L., and Maceli, N., 2019. "Investigation on low-pressure steam turbine exhaust hood modelling through computational fluid dynamic simulations". In AIP Conference Proceedings, Vol. 2191, AIP Publishing LLC, p. 020076.

[42] Alekseenko, S., Kuibin, P., Okulov, V. L., and Shtork, S., 1999. "Helical vortices in swirl flow". *Journal of Fluid Mechanics,* ***382***, pp. 195–243.

